PCCP

ROYAL SOCIETY OF CHEMISTRY

PAPER

View Article Online
View Journal

Cite this: DOI: 10.1039/d5cp04426j

Steady-state and time-resolved near-infrared photoluminescence of $[M_1Ag_{24}(SR)_{18}]^{n-}$ (M = Ag, Au, Pt, Pd, Ni) nanoclusters

Usama Tash, Weijie Ji, Avirup Sardar, Yitong Wang and Rongchao Jin *

Received 15th November 2025,
Accepted 12th February 2026

DOI: 10.1039/d5cp04426j

rsc.li/pccp

Silver nanoclusters (NCs) of atomic precision are attractive in terms of optical properties, and among the reported NCs, the thiolate (SR)-protected $[Ag_{25}(SR)_{18}]^-$ serves as a model system for uncovering how the electronic structure dictates light emission. Here, we examine the effect of substituting the central Ag atom in $[Ag_{25}(SR)_{18}]^-$ with Au, Pt, Pd, or Ni (note: 2− charge for Pt, Pd and Ni doped NCs). Combining steady-state, time-resolved, and oxygen-dependent photoluminescence (PL) spectroscopic studies, we show that dopants introduce distinct electronic effects that affect optical absorption and emission, and that all cases exhibit predominant phosphorescence in the near-infrared region. The incorporation of isoelectronic gold greatly enhances radiative triplet emission, yielding an unusually high quantum yield, whereas Pt or Pd substitution favors nonradiative decay despite retaining the 8-electron closed–shell superatomic configuration by charge compensation. Finally, Ni doping produces a redshift in luminescence while the other dopants lead to a blueshift compared to that of Ag_{25}. Taken together, these results reveal how single-atom substitution modulates both radiative and nonradiative pathways, establishing the doped MAg_{24} nanoclusters as a versatile platform for tuning near-infrared photophysics at the atomic level.

Introduction

Atomically precise metal nanoclusters (NCs) contain a specific number of atoms in the range of tens to hundreds of metal atoms per core and have received wide interest.[1–11] A prototypical example is the 25-atom gold NC with a formula of $[Au_{25}(SR)_{18}]^-$ (where SR = thiolate), which possesses a well-defined icosahedral Au_{13} core and six dimeric staple-like motifs (–SR–Au–SR–Au–SR–), exhibiting a closed–shell superatom electronic configuration ($1S^21P^6$) with 8 delocalized valence electrons in the core.[12] For its silver analogue, Joshi *et al.*[13] later reported $[Ag_{25}(SR)_{18}]^-$ (abbreviated as Ag_{25}), which was found to be isostructural with $[Au_{25}(SR)_{18}]^-$, not only in the geometric structure, but also the superatomic electronic structure. This equivalence enables a direct comparison of the photophysical properties of Ag- and Au-based superatoms within an identical coordination environment.

Building on the Ag_{25} NC, researchers have explored single-atom doping with various heterometals (M) to tune the properties, including both experimental[14–21] and theoretical work.[22–27] Experimentally, Bakr and co-workers[14] achieved doping of Ag_{25} with one Au atom *via* galvanic exchange, yielding a $[AuAg_{24}(SR)_{18}]^-$ product. The crystal structure of this $AuAg_{24}$ NC revealed an icosahedral $M@Ag_{12}$ core analogous to that in the parent Ag_{25}, with the Au atom occupying the central site of the icosahedron. Zheng and co-workers reported the Pd- and Pt-doped ones, *i.e.*, $[PdAg_{24}(SR)_{18}]^{2-}$ and $[PtAg_{24}(SR)_{18}]^{2-}$, and single-crystal X-ray diffraction (XRD) showed that both $PdAg_{24}$ and $PtAg_{24}$ preserve the same framework as $[Au_{25}(SR)_{18}]^-$, *i.e.*, consisting of an M-centered Ag_{12} icosahedral core capped by six $Ag_2(SR)_3$ staples.[15] In these heteroatom-doped systems, the dopant's different valence necessitates a change in the NC charge: for example, doping $[Ag_{25}]^-$ with a Pt converts the nanocluster to a 2− charge in order to maintain an 8-electron superatom configuration.[15] Recently, Ni-doping of Ag_{25} has also been achieved *via* a metal-exchange strategy, producing a $[NiAg_{24}(SPhMe_2)_{18}]^0$ NC and its two-electron reduced derivative $[NiAg_{24}(SPhMe_2)_{18}]^{2-}$.[16] In the neutral $NiAg_{24}$, the Ni substitution gives a 6-electron open–shell superatom that undergoes Jahn–Teller distortion, whereas upon reduction to the 2− state it becomes a stable 8-electron closed–shell superatom with an undistorted, isotropic core (confirmed by single-crystal XRD).[16] In the cases of Au, Pt and Pd doping, the groups of Wu, Zhu and Patra have reported the PL[18,19] and ultrafast dynamics[21] studies. Theoretically, accurate electronic structure analysis,[22–25] absorption spectra,[22] HOMO–LUMO gap,[25] PL mechanism,[26] and vibrational modes[27] of $MAg_{24}(SR)_{18}$ with M = Ag, Au, Pt, and Pd have been tackled by several groups. All these studies have provided a

Department of Chemistry, Carnegie Mellon University, Pittsburgh, Pennsylvania 15213, USA. E-mail: rongchao@andrew.cmu.edu

fundamental understanding of how single-atom dopants alter the electronic structure of superatomic silver NCs.

Single-atom substitution provides a tunable platform to dissect the photoluminescence (PL) mechanisms. In addition to Au, Pt, Pd, and Ni, recent work by Lee and coworkers also succeeded in doping Ag_{25} with open d-shell Ru, Os, or Ir in the form of metal hydride (*i.e.*, RuH_2, OsH_2, IrH, all being d^{10} with the incorporation of hydrides), and PL mechanistic studies revealed that dopants modulate both the radiative and non-radiative decay channels.[28]

Studying the PL of both undoped and doped metal NCs provides crucial insight into how atomic and electronic structures dictate light emission. The structure–emission correlations will establish a general design framework for tailoring optical properties across nanocluster systems. Although Ag_{25} and the doped MAg_{24} (M = Au, Pt, Pd, Ni) nanoclusters have been previously studied for their PL characteristics, those works primarily focused on qualitative emission behavior and steady-state measurements, with the lifetime information missing (note: recent work by Maity *et al.*[21] probed the lifetimes of M = Ag, Au, Pt and Pd cases, but Ni was still missing). The lifetime information is critical for understanding the PL mechanism.[29,30] Several key questions also remain unresolved—particularly regarding the contributions of fluorescence, phosphorescence, and thermally activated delayed fluorescence (TADF).[28] Moreover, the quantitative relationship between radiative and nonradiative decay channels has not been firmly established, and the excited-state lifetimes of the MAg_{24} series have not been systematically measured or compared under identical conditions. The present study therefore revisits the Ag_{25} series with unified steady-state, time-resolved, and oxygen-dependent analyses, providing insights into the doping effects and PL mechanism.

Here, we report a detailed investigation on $[Ag_{25}(SR)_{18}]^-$ and its doped analogues $[MAg_{24}(SR)_{18}]^{n-}$ (M = Au, Pt, Pd, Ni) by integrating steady-state with time-resolved and oxygen-dependent PL measurements. By correlating the valence electron count, HOMO–LUMO gap (E_g) modulation, and spin–orbit coupling with changes in PL quantum yield (QY), emission energy, and excited-state lifetimes, this work aims to establish a framework for dopant-controlled emission tuning in superatomic nanoclusters. The single-atom dopants drastically alter the QY from the highest 30.6% for $AuAg_{24}$ to strong quenching in $PtAg_{24}$ and confirm that the emission arises predominantly from long-lived triplet state, as evidenced by microsecond (μs) lifetimes and O_2 quenching of the PL.

Results and discussion

The syntheses of $[Ag_{25}(SR)_{18}]^-$ and $[MAg_{24}(SR)_{18}]^{n-}$ (M = Au, Pt, Pd, Ni) followed the literature reports.[13,16] To ensure the purity of samples, we first crystallized all NCs, and the re-dissolved crystals were used in the spectroscopic measurements. In addition, the PL of metal NCs is often quite broad (spanning the entire near-infrared (NIR) range, ~700 to 1700 nm, depending on the size and composition), thus, we introduced a broadband InGaAs photomultiplier detector for both the stead-state and time-resolved measurements.[29,30]

Doping effect on HOMO–LUMO gap and superatomic electron configuration

The homometal and doped NCs' optical absorption spectra are shown in Fig. 1; the photon energy scale spectra are shown in Fig. S1. Same as the Au_{25} NC,[12] homometallic Ag_{25} is a closed–shell superatom[22–27] with 8 delocalized electrons ($1S^21P^6$) and possesses an E_g of ~1.48 eV (the onset of absorbance, Fig. S1), which serves as the basis for comparison with the doped NCs. Replacing one Ag with Au, Pt, Pd, or Ni may alter the electron count and modifies the electronic distribution within the icosahedral core. Below we discuss the four doping cases and their effects.

Au doping (M = Au). In $[AuAg_{24}(SR)_{18}]^-$, the single Au atom occupies the central site of the Ag_{13} icosahedral core, as confirmed by single-crystal XRD and extended X-ray absorption fine structure (EXAFS) analyses.[14] The central Au does not change the total superatomic electron count from that of the parent $[Ag_{25}(SR)_{18}]^-$. Both have the 8-electron closed–shell ($1S^21P^6$) configuration, and their E_g values are similar (Fig. S1 and Table 1), so are the optical absorption profiles.

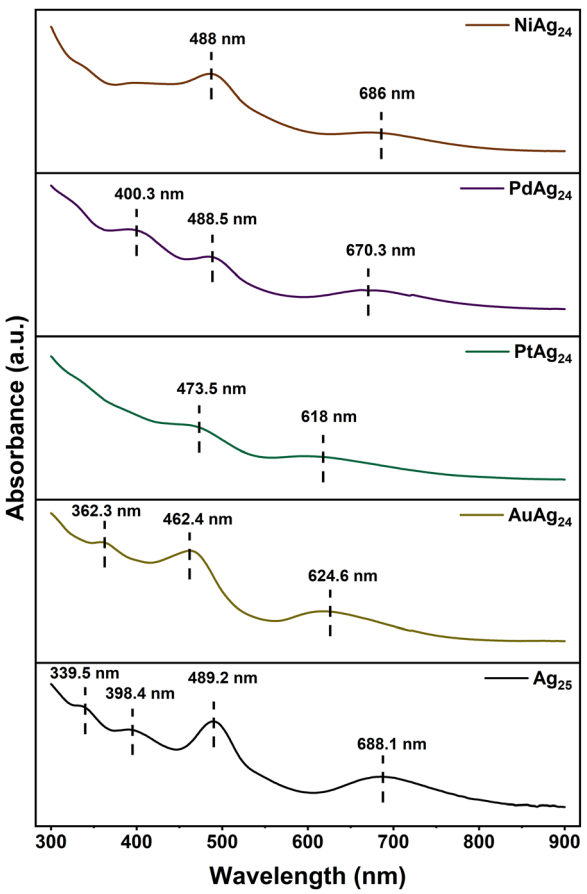

Fig. 1 UV-vis absorption spectra of $[Ag_{25}(2,4\text{-DMBT})_{18}]^-$ and $[MAg_{24}(2,4\text{-DMBT})_{18}]^{n-}$ (M = Au, Pt, Pd, Ni) in $CDCl_3$ at room temperature. The cluster charge ($n-$) is 1- for Au, 2- for Pt, Pd, and Ni.

Table 1 Summary of E_g and valence electron configurations for Ag_{25} and MAg_{24} (M = Au, Pt, Pd, Ni) NCs

Sample	E_g (eV)	Atom valence electron configuration	Central atom within the NC	Dopant's contribution to the NC's free valence electrons
$[Ag_{25}(SR)_{18}]^-$	1.48	Ag, Z = 47 $[Kr]4d^{10}5s^1$	No change	1
$[AuAg_{24}(SR)_{18}]^-$	1.47	Au, Z = 79 $[Xe]\ 5d^{10}6s^1$	No change	1
$[PtAg_{24}(SR)_{18}]^{2-}$	1.45	Pt, Z = 78 $[Xe]\ 5d^96s^1$	$5d^{10}6s^0$	0
$[PdAg_{24}(SR)_{18}]^{2-}$	1.49	Pd, Z = 46 $[Kr]\ 4d^{10}5s^0$	No change	0
$[NiAg_{24}(SR)_{18}]^{2-}$	1.41	Ni, Z = 28 $[Ar]\ 3d^84s^2$	$3d^{10}4s^0$	0

Pt and Pd doping (M = Pt, Pd). The central Ag atom contributes one 5s valence electron to the superatomic HOMO, but Pt or Pd behaves as a "zero-electron" dopant (d^{10}), donating no electron to the superatomic orbitals, thus, effectively removing one electron. To compensate and preserve the closed–shell superatomic configuration, the NC must carry an extra negative charge compared to the original $[Ag_{25}(SR)_{18}]^-$. Thus, the doped NCs are isolated as 2- anions, $[PtAg_{24}(SR)_{18}]^{2-}$ and $[PdAg_{24}(SR)_{18}]^{2-}$, which satisfies the 8-electron count: total superatomic electrons = 24 (Ag) + 0 (Pt or Pd) + 2 (from 2− charges) − 18 (thiolates) = 8.[15,19] Of note, Pd and Pt atoms exhibit electronic configurations of $[Kr]4d^{10}5s^0$ and $[Xe]4f^{14}5d^96s^1$, respectively, but within the NC, both dopants adopt a closed–shell $d^{10}s^0$ electron configuration, characterized by fully filled d-orbital and vacant s-orbital, thus, contributing no electron to the superatomic orbitals (Table 1).

Ni doping (M = Ni). Ni locates in the same group of Pd and Pt but is much more reactive. Ni doping leads to an electron-deficient NC unless charge compensation is provided. A single Ni substituent fails to supply electrons to the superatomic orbitals; however, because Ni is less noble than Ag, the as-synthesized Ni-doped NC emerges in a higher oxidation state (neutral overall), instead of being further reduced. The initial product $[NiAg_{24}(SR)_{18}]^0$ contains only 6 superatomic electrons ($1S^21P^4$).[16] This $6e^-$ configuration leaves the 1P shell only partially filled and accordingly induces a Jahn–Teller distortion of the $NiAg_{12}$ core, as observed in its crystallographic structure.[16] Upon two-electron reduction, however, the Ni-doped NC can be switched to a closed–shell state: addition of two electrons yields $[NiAg_{24}(SR)_{18}]^{2-}$, which restores the full $1S^21P^6$ superatomic configuration ($8e^-$) and thereby reverts the NC to an undistorted, ideal icosahedral geometry. X-ray analysis confirms that the reduced $NiAg_{24}$ core becomes isotropic and superimposable with the Pt/Pd analogues once the 8-electron shell is achieved. This reversible interconversion between a distorted geometry of 6-electron state and a symmetric geometry of 8-electron state is a unique feature of Ni doping, enabling a charge-state switching in the cluster. Experimentally, $NiAg_{24}$ can exist in both neutral (open–shell, $6e^-$) and doubly anionic (closed–shell, $8e^-$) forms, depending on its redox state.[16] Of note, the photophysical measurements in this study were performed on the reduced $[NiAg_{24}(SR)_{18}]^{2-}$ (Table 1).

Taken together, the doping effects on the NC charge, E_g, and superatomic electron configuration are summarized in Table 1. When Au replaces the central Ag atom, it preserves the 8-electron closed shell, leaving E_g essentially unchanged. To maintain an 8-electron shell closure, Pt or Pd doped NCs adjust their charge accordingly and do not alter the E_g due to the preserved $8e^-$ configuration, whereas Ni can cause the cluster to have either 6 or 8 electrons, depending on its oxidation state. This change in electron filling alters the frontier orbital occupancy and the E_g value, and excited state relaxation behavior for the Ni doped case.[16,25] Of note, the Ni doping effect in Ag_{25} is similar to the case of Ni-doping in Ag_{29}.[31]

Photoluminescence and quantum yields

Steady-state PL measurements (Fig. 2A) in He-degassed solutions reveal clear dopant-dependent effects. The NIR emission (peaks in 900–1020 nm) differs from earlier reports (peaks around 800 nm).[18,19,21] Among the dopants, replacing the central Ag atom with Ni produces a similar peak wavelength (~1024 nm) compared to Ag_{25} (peak ~1017 nm), whereas Pt

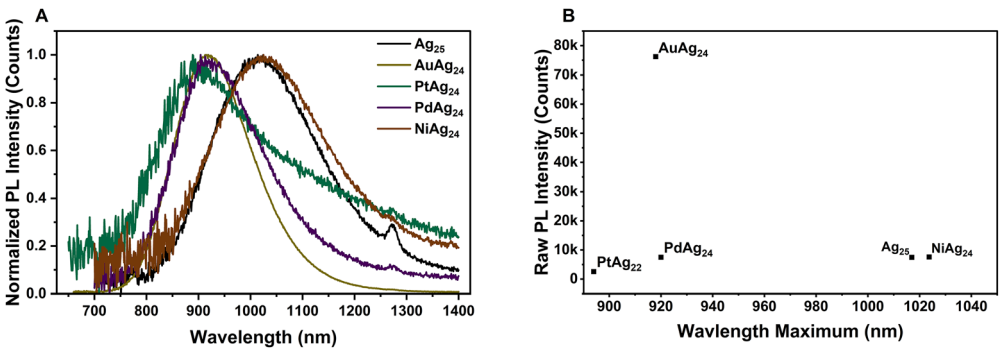

Fig. 2 (A) Normalized PL spectra of $[Ag_{25}(2,4\text{-DMBT})_{18}]^-$ and $[MAg_{24}(2,4\text{-DMBT})_{18}]^{n-}$ (M = Au, Pt, Pd, Ni) NCs under He. (B) Emission intensities *versus* peak wavelengths for the dopant cases.

substitution yields the most blueshift (peak ~894 nm); Au- and Pd-doped ones emit at intermediate wavelengths in the ~918–920 nm range, Fig. 2B.

Since the MAg_{24} series exhibits comparable optical gaps ($E_g \approx$ 1.4–1.5 eV), the PL peak shifts are best explained by dopant-dependent excited-state relaxation (Stokes shift) rather than differences in the absorption gap alone. Importantly, the Ni-doped cluster studied here is the reduced species $[NiAg_{24}(SPhMe_2)_{18}]^{2-}$, which has an $8e^-$ closed–shell superatomic configuration ($1S^21P^6$). We therefore attribute the Ni red-shift to greater structural and vibrational relaxation after excitation: the 3d Ni dopant strengthens the coupling between the excited electrons and the cluster's vibrations, allowing more energy to be lost as vibrational motions before emission. As a result, emission occurs from a more relaxed (lower-energy) excited state, giving rise to a larger Stokes shift and thus lower-energy (more red-shifted) PL.

The most striking effect of doping pertains to the photoluminescence quantum yield (PLQY), Fig. 3. The PL spectral measurements were carried out in deaerated solutions (He purged) to remove the dissolved O_2, which is a well-known quencher of triplet excited states. All samples were measured in deuterated chloroform ($CDCl_3$) as the solvent to eliminate solvent absorption of PL. The undoped Ag_{25} exhibits a PLQY of ~3.5%. Introducing a single Au atom into Ag_{25} significantly boosts the PLQY by an order of magnitude, whereas adding a Pt atom drastically quenches PL. Specifically, the PLQY of $AuAg_{24}$ is ~30.6%, similar to previous reports,[30,32] an exceptionally high value for NCs at room temperature. Pd doping yields a modestly enhanced PLQY (4.1%), and Ni doping with ~3.2%. The $PtAg_{24}$ NC shows the lowest PLQY (only ~1.5%). These results indicate that Au doping is uniquely effective at enhancing radiative efficiency (*vide infra*), whereas a Pt dopant is detrimental to the PL. The ~30.6% QY of $AuAg_{24}$ is one of the highest ever reported for NCs in solution at room temperature, *cf.*, the prototypical $[Au_{25}(PET)_{18}]^-$ has a PLQY of ~1%.[30] The 30.6% yield also rivals or exceeds other reported values achieved by surface or aggregation engineering, *e.g.* ~8% in aggregated Au_{22} clusters[33] or ~15% in certain ligand-exchanged Au_{25}-rod derivatives,[34] underscoring the remarkable impact of the single Au dopant. The $AuAg_{24}$ appears to provide an ideal combination of electronic and structural factors that maximize radiative recombination (see more discussions below).

PL lifetimes and mechanistic insights

Time-resolved photoluminescence decay measurements in the nanosecond (ns) to microsecond (μs) timescales provide insight into the nature of the emissive states in the NCs.[21,28–30]

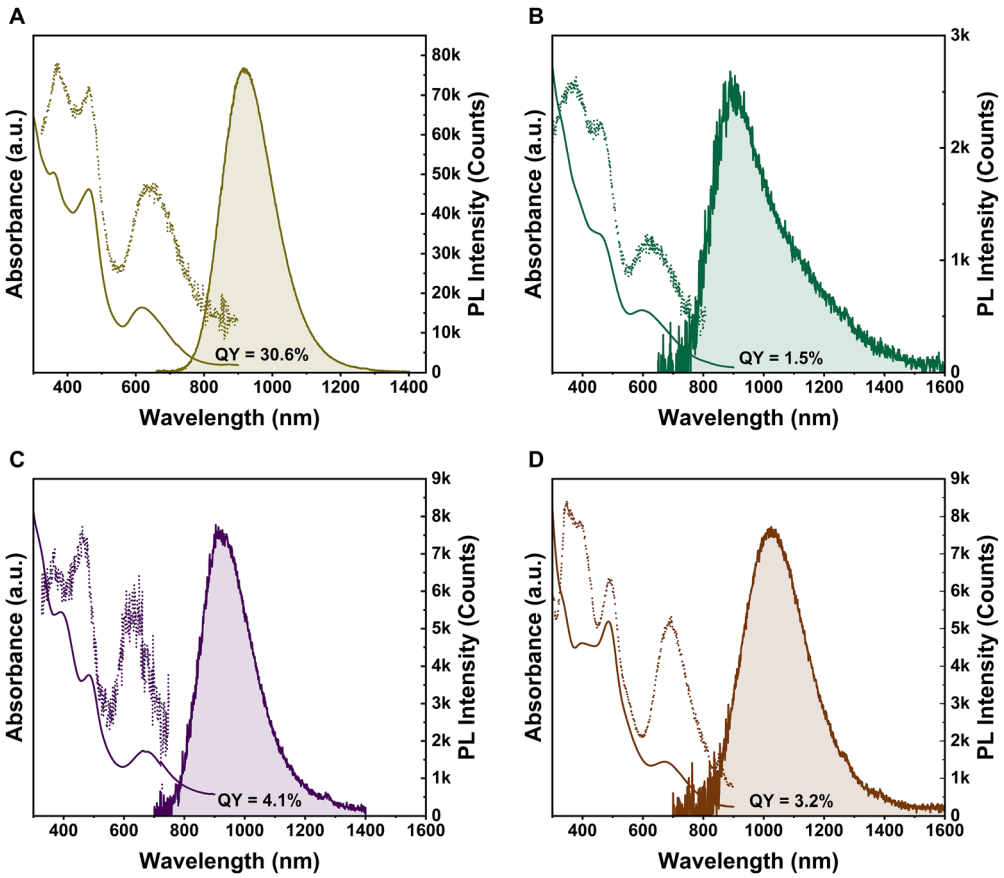

Fig. 3 UV-vis absorption (solid lines), PL (shaded) and excitation (PLE, dotted lines) spectra of $[MAg_{24}(2,4\text{-}DMBT)_{18}]^{n-}$ (M = Au, Pt, Pd, Ni) nanoclusters in $CDCl_3$ at 298 K. Panels A–D correspond to $AuAg_{24}$, $PtAg_{24}$, $PdAg_{24}$, and $NiAg_{24}$, respectively. The PLQYs are indicated in each panel.

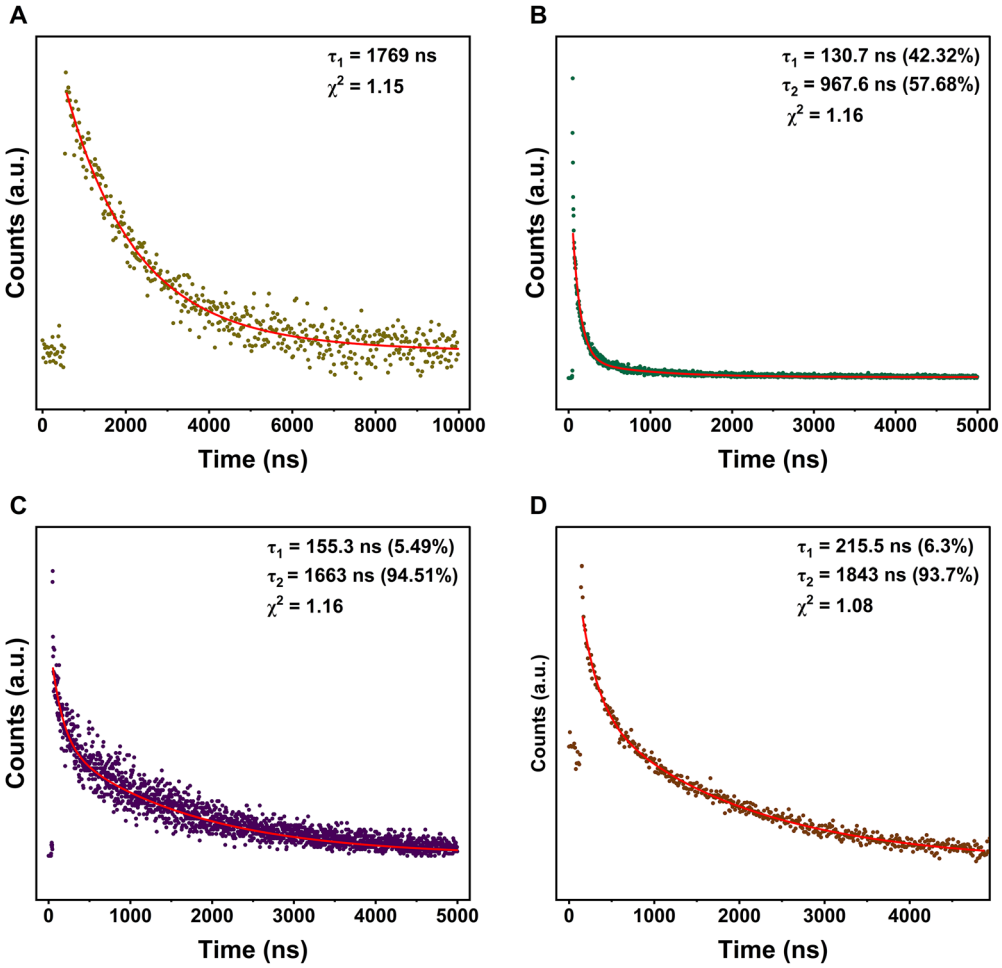

Fig. 4 Time-resolved PL decay profiles of $[MAg_{24}(2,4\text{-DMBT})_{18}]^{n-}$ (M = Au, Pt, Pd, Ni) NCs under He atmosphere. Panels A–D correspond to $AuAg_{24}$, $PtAg_{24}$, $PdAg_{24}$, and $NiAg_{24}$, respectively. Red traces represent biexponential fits with lifetimes (τ_1, τ_2) and corresponding amplitudes (%) shown in each panel.

Fig. 4 displays the PL decay profiles of the doped NCs (recorded under He inert atmosphere). The PL decays can be well fitted ($\chi^2 \approx 1.08$–1.16) using a bi-exponential function: $I(t) = I_0 + A_1e^{(-t/\tau_1)} + A_2e^{(-t/\tau_2)}$, where I_0 is the time-zero intensity (or baseline), τ_1 and τ_2 represent the short- and long-lived lifetimes, and A_1 and A_2 are the amplitudes (%). The extracted lifetimes and their amplitudes are listed in Table 2. The bi-exponential decay behavior observed in the series indicates the presence of two distinct emissive components.

Under helium at ambient temperature for all doped NCs, $AuAg_{24}$ shows a single-exponential decay with a lifetime of 1.769 μs (Fig. 4A), indicative of triplet-state T_1 emission (*i.e.* phosphorescence). The measured lifetime matches the value reported by Maity *et al.* previously.[21,35] $PtAg_{24}$ (Fig. 4B) displays mixed character, with a TADF channel (τ_1 = 130.7 ns, 42.32%) alongside triplet emission (τ_2 = 967.6 ns, 57.68%). Its triplet state involvement is further substantiated by O_2-induced PL quenching and concomitant $^1O_2$ generation (*vide infra*). In addition to the biexponential lifetime behavior, spectral deconvolution of the $PtAg_{24}$ emission (Fig. 5) reveals two distinct emissive components, consistent with the overlapped singlet (S_1) and triplet (T_1) contributions. Therefore, both TADF

Table 2 Summary of photoluminescence parameters (peak λ_{max}, quantum yield, lifetime components and average lifetime) and the derived radiative (k_r) and non-radiative (k_{nr}) decay rates for Ag_{25} and MAg_{24} nanoclusters (helium purged)

NC	PL λ_{max} (nm)	PLQY (%)	τ_1 (A_1) ns	τ_2 (A_2) ns	Average τ* ns	k_r (s^{-1})	k_{nr} (s^{-1})
Ag_{25} (ref. 30)	1017	3.5	—	1100 (100%)	1100	3.18×10^4	8.77×10^5
$AuAg_{24}$	918	30.6	—	1769 (100%)	1769	1.73×10^5	3.92×10^5
$PtAg_{24}$	894	1.5	131 (42.3%)	967 (57.7%)	613	2.45×10^4	1.61×10^6
$PdAg_{24}$	920	4.1	155 (5.5%)	1663 (94.5%)	1580	2.59×10^4	6.07×10^5
$NiAg_{24}$	1024	3.2	215 (6.3%)	1843 (93.7%)	1740	1.84×10^4	5.56×10^5

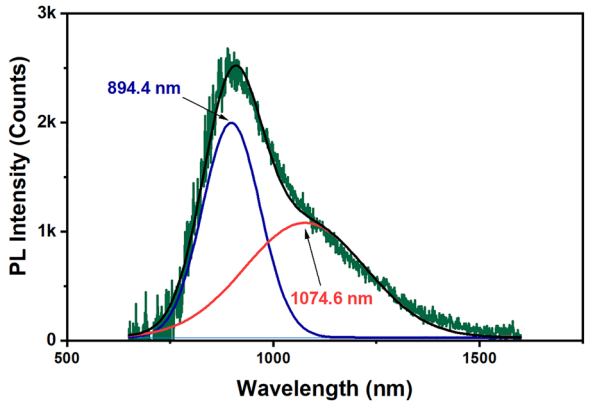

Fig. 5 Spectral deconvolution of $PtAg_{24}$ emission into singlet (blue profile) and triplet (red) contributions.

(shorter wavelength due to higher energy, centered at 894 nm) and phosphorescence (longer wavelength, centered at 1075 nm), with a S_1–T_1 peak splitting of 0.23 eV (estimated by the peak energy difference). $PdAg_{24}$ (Fig. 4C) is triplet-dominated (1.663 μs, 94.51%) with a minor TADF emission (155.3 ns, 5.49%). $NiAg_{24}$ (Fig. 4D) also exhibits mainly triplet-derived emission (1.843 μs, 93.70%) with a small TADF (215.5 ns, 6.30%). Overall, Au, Pd, and Ni doped MAg_{24} NCs all feature triplet-derived emission, whereas Pt retains a large (roughly half) contribution from $\sim 10^2$ ns delayed fluorescence. For the Ag_{25} and Au/Pd/Ni doped four NCs, their PL peaks are reasonably symmetric, indicating a much smaller S_1–T_1 splitting (estimated $\sim$0.1 eV or so).

For $PtAg_{24}$, spectral deconvolution suggests an S_1–T_1 peak splitting $\Delta E_{ST} \approx 0.23$ eV. This value is larger than that of highly efficient TADF emitters, therefore, the delayed-fluorescence contribution in $PtAg_{24}$ is expected to be modest; but other factors may promote revserse intersystem crossing (RISC), such as spin–orbit coupling and reorganization energy, which are unknown yet and require future theoretical evaluation. In addition, because TADF originates from thermally assisted reverse intersystem crossing ($T_1 \rightarrow S_1$), the most direct validation of TADF is its temperature dependence, where the delayed fluorescence increases with temperature but is suppressed at low temperatures. In the present work, the room-temperature biexponential decay and spectral deconvolution support a delayed-fluorescence component overlapping with triplet emission, but definitive evidence for TADF will require temperature-dependent PL measurements, which remain to be tested.

The quantum yield enhancement and quenching observed above are further analyzed by calculating the radiative (k_r) and nonradiative (k_{nr}) decay rate constants using eqn (1)–(3) below.

$$\Phi = \tau^* k_r \quad (1)$$

$$\tau^* = \frac{\sum_i A_i \tau_i}{\sum_i A_i} \quad (2)$$

$$\Phi = \frac{k_r}{k_r + k_{nr}} \quad (3)$$

where, Φ is the measured PLQY, τ^* is the amplitude-weighted average lifetime (eqn (2)), and A_i and τ_i are the amplitude and lifetime of component i. The calculated results are listed in Table 2, together with other PL parameters extracted from Fig. 3.

In previous work by Lee and coworker, the radiative rate was correlated with the dopant's electron affinity (and associated superatomic orbital energy shifts) or spin–orbit coupling, while nonradiative losses were found to be governed by how the core structure and vibrations are altered upon doping.[28] Herein we performed a detailed analysis of k_r and k_{nr}, and found that $AuAg_{24}$ uniquely combines a higher k_r and lower k_{nr} ($k_r = 1.73 \times 10^5$ s^{-1}, $k_{nr} = 3.92 \times 10^5$ s^{-1}) than the homometallic Ag_{25} (Table 2) yielding the highest QY (30.6%). The lower k_{nr} can be attributed to the rigidifying effect of Au substitution into the icosahedral core, which suppresses electron–phonon coupling.[30] As shown in Fig. 6, the average Ag–Ag bond lengths in $AuAg_{24}$ and Ag_{25} are nearly identical; however, Ag_{25} exhibits more pronounced fluctuations in its radial bond-length distribution,

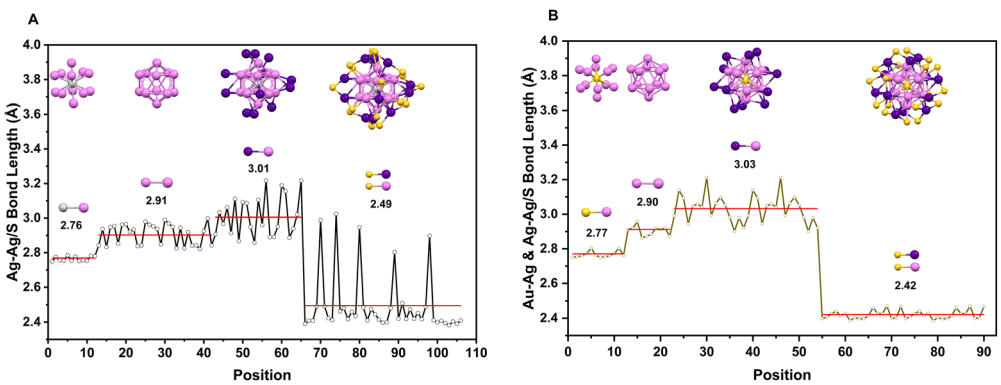

Fig. 6 Radial bond-length distribution of Ag–Ag/S in (A) $[Ag_{25}(2,4\text{-DMBT})_{18}]^-$ and (B) $[AuAg_{24}(2,4\text{-DMBT})_{18}]^-$ nanoclusters. Each panel shows the measured Ag–Ag/S distances *versus* atomic position, highlighting distinct bond-length regions corresponding to center–shell, shell–shell, and surface–staple atoms. Color code: silver (central Ag in A), gold (central Au in B), violet (icosahedral Ag atoms in A/B), blue (peripheral Ag in A/B), and yellow (thiolate S; large yellow sphere in B = central Au).

indicating greater structural flexibility. In contrast, Au incorporation slightly compresses the core and markedly reduces bond-length dispersion, yielding a more rigid framework. This enhanced rigidity in $AuAg_{24}$ minimizes vibrational relaxation pathways, thereby lowering nonradiative decay and increasing overall photoluminescence efficiency. Compared to Ag_{25}, $PtAg_{24}$ exhibits a similar k_r but a markedly elevated k_{nr} (1.61×10^6 s^{-1}), which explains its lower Φ (1.5%), thus, Pt doping quenches PL, with the nonradiative channels arising from enhanced vibronic coupling. $PdAg_{24}$ shows a modest improvement in Φ (4.1%) driven primarily by a reduction in k_{nr} (6.07×10^5 s^{-1}) with only a minor change in k_r. $NiAg_{24}$ shows both reduced rates ($k_r = 1.84 \times 10^4$ s^{-1}, $k_{nr} = 5.56 \times 10^5$ s^{-1}); such a counteracting effect yields a Φ similar to that of Ag_{25}.

With respect to the dopants (Pt, Pd, Ni), both Pt and Pd cases show a slight contraction in the average M-Ag_{12} radial bond length (2.752 Å (Pt) and 2.747 Å (Pd) *vs.* 2.764 Å for homosilver), and the Ni case has the most compact kernel (average radial bond length: 2.706 Å) due to its smallest atomic radius. Compared to the slight increase in the PL for Pd doping and slight decrease for Ni doping, the observed marked PL quenching in Pt dopant may be explained by counteracting from the stronger *d-s* electronic interactions in the Pt case, resulting in stronger nonradiative decay. In comparison, both Au and Ag have d^{10} configuration and their *d*-shell is quite inert, thus, the $AuAg_{24}$ and Ag_{25} cases have higher PL than the Pt doping case.

Effect of O_2 on the PL

In the MAg_{24} series, molecular oxygen ($^3O_2$ for its ground state) efficiently quenches the PL of NCs due to photosensitization-induced generation of excited-state oxygen, *e.g.*, singlet oxygen ($^1O_2$), thus, it can be used to confirm the triplet-state nature of the emission (phosphorescence).[36] For $AuAg_{24}$, the QY drops from 30.6% (under He) to 22.9% (under O_2)—a ~25% decrease (Fig. 7A)—and the amplitude-weighted lifetime shortens from 1.769 to 1.598 μs (Fig. 8A), consistent with the efficient intersystem crossing (ISC) and triplet emission.[36,37] $PtAg_{24}$ exhibits a PL quenching from 1.5% to 1.1% (~27% variation; Fig. 7B), accompanied by a pronounced lifetime (τ_2) shortening from 0.968 to 0.509 μs (Fig. 8B), evidencing triplet states of sufficient lifetime for oxygen sensitization. $PdAg_{24}$ shows an even stronger response to O_2: QY decreases from 4.1% to 1.5% (~63% variation; Fig. 7C) and τ_2 drops from 1.66 to 1.14 μs (Fig. 8C), indicating extensive triplet state energy transfer to O_2. $NiAg_{24}$ also shows strong QY quenching, 3.2% to 1.1% (~66% variation, Fig. 7D), while its τ_2 changes only modestly, Fig. 8D. The coordinated intensity drop and lifetime shortening under O_2 substantiate the triplet-state character of the emission for the

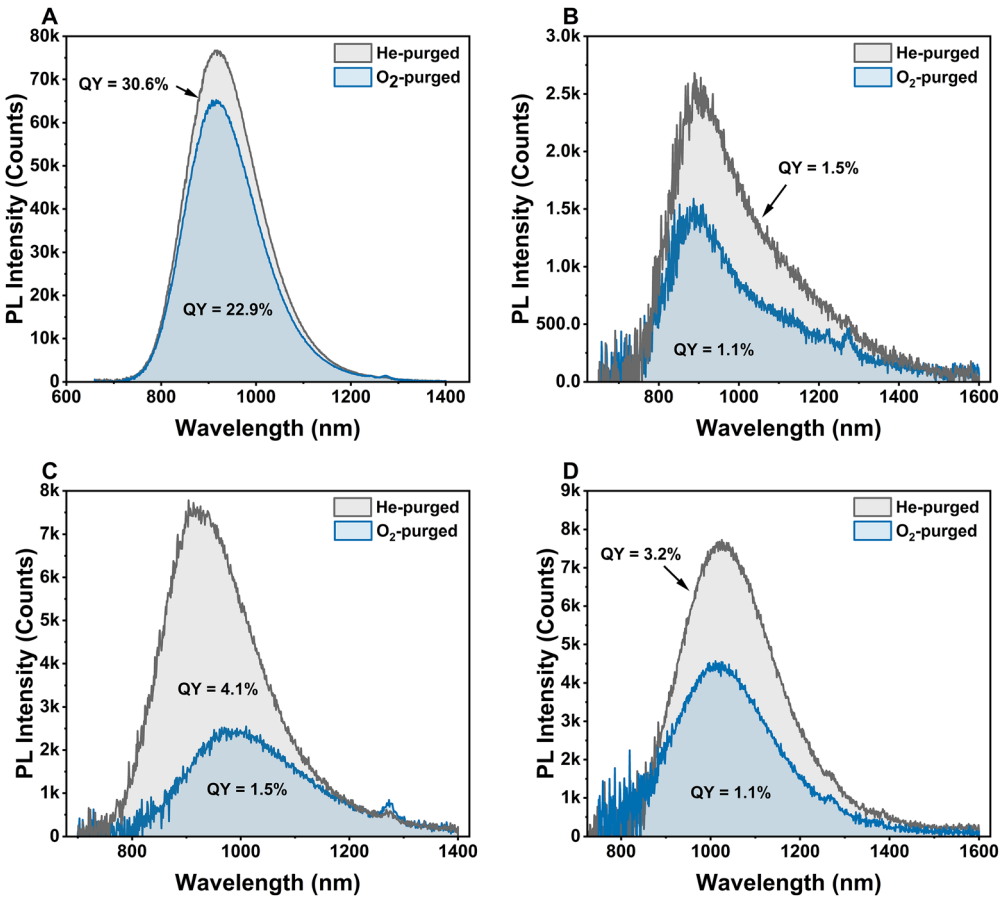

Fig. 7 Oxygen sensitization by $AuAg_{24}$ (A), $PtAg_{24}$ (B), $PdAg_{24}$ (C), and $NiAg_{24}$ (D) showing PL quenching upon O_2 purging compared to He-purged conditions.

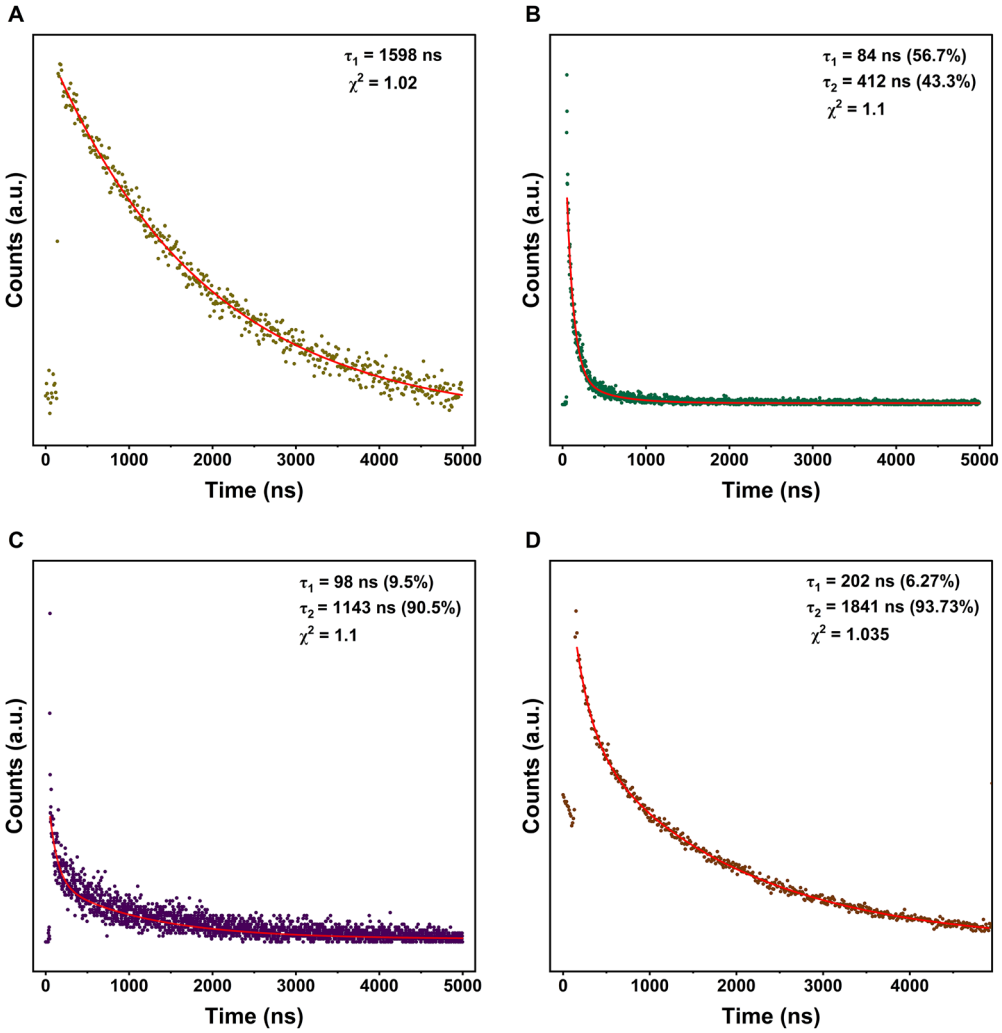

Fig. 8 Time-resolved PL decay curves of $AuAg_{24}$ (A), $PtAg_{24}$ (B), $PdAg_{24}$ (C), and $NiAg_{24}$ (D). All solutions were bubbled with O_2.

doped NC series. In addition, all cases show a small emission peak at 1275 nm, which is characteristic of the emission of $^1O_2$ produced (Fig. 7). Overall, the O_2 test indicates the involvement of triplet state in the PL process of all the NCs.

In purely dynamic (collisional) quenching, O_2 acts after excitation by introducing an additional nonradiative deactivation pathway, so the PL intensity and excited-state lifetime typically drop. In the Ni doping case, the intensity decreases while the lifetime remains unchanged, indicating a different mechanism. We rationalize that the highly reactive $[NiAg_{24}(SR)_{18}]^{2-}$ NCs were partially oxidized to $[NiAg_{24}(SR)_{18}]^0$ ($E_g \sim 0.76$ eV or 1630 nm wavelength, see ref. 16), and if one considers a Stokes shift, its emission (if any) would be far beyond 1700 nm (our detector's limit). For such a small gap, we predict the oxidized NCs would not be emissive; rather, it would show predominantly nonradiative decay. Since the amount of O_2 in the solution is limited, not all $[NiAg_{24}(SR)_{18}]^{2-}$ were oxidized, thus, the survived portion (2− charge state) still showed the same lifetime. Overall, this abnormal case should be related to the high reactivity of $[NiAg_{24}(SR)_{18}]^{2-}$ compared to the other cases that are much less reactive with O_2 due to noble metal doping.

PL mechanism

Based on the above results and analysis, we summarize the PL mechanism in Scheme 1. Following photoexcitation, the exciton first relaxes to the lowest excited state (S_1), from which ISC to the T_1 state occurs, and accordingly the T_1 state gets populated. We estimate the direct S_1 emission prior to ISC is minor since no PL lifetime within the range of a few nanoseconds was detected, unlike the case of $Au_{42}(SR)_{32}$ quantum rods in which strong fluorescence (lifetime < 1 ns) was observed.[38] The range of tens of ns to one to two hundreds of ns is attributed to the TADF component,[30] whereas the microsecond component typically arises from phosphorescence. With this mechanism, all the five NCs emit predominant phosphorescence, with less from TADF. Except the case of $PtAg_{24}$, the S_1 and T_1 energies for other cases are very close since no split peaks are found in their PL spectra, unlike the case of

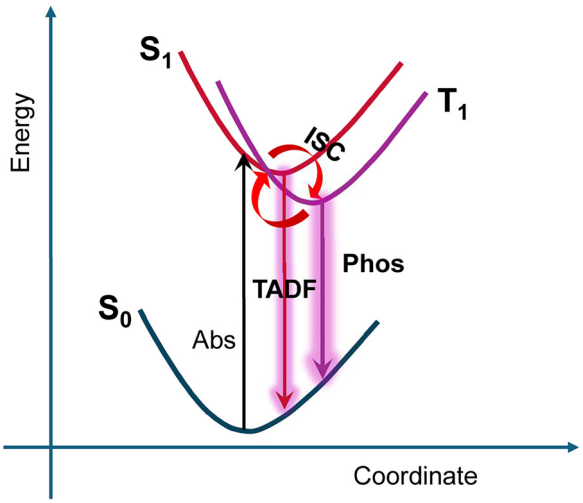

Scheme 1 PL mechanism for Ag_{25} and MAg_{24} nanoclusters.

$Au_{42}(SR)_{32}$ quantum rod in which the fluorescence and the phosphorescence are distinctly split into two peaks.[38–40]

Compared to previous reports,[14–21] our current work has contributed to the following aspects: (i) the entire Ag_{25}/MAg_{24} (Au, Pt, Pd, Ni) series is characterized by unified steady-state and time-resolved PL, as well as oxygen triplet sensitization under the same experimental conditions; (ii) systematic extraction and comparison of k_r and k_{nr} across all dopants by consistent analysis of lifetime/QY; and (iii) inclusion of $NiAg_{24}$ in the same mechanistic framework, enabling direct comparison with Au/Pt/Pd in terms of electron counts, emission shifts, and quenching behavior. Together, these efforts provide a quantitative dopant-dependent mapping of radiative *vs.* nonradiative pathways that was not previously established as a complete, consistent dataset in earlier reports.

Conclusions

In summary, doping a single heteroatom into the $[Ag_{25}(SR)_{18}]^-$ nanocluster provides a powerful means of tuning its electronic and photophysical properties. Gold substitution preserves the closed–shell electron count ($8e^-$) and rigidifies the core, thus, giving rise to a high PLQY of 30.6% through significantly enhanced triplet emission. Doping by Pt or Pd maintains the 8-electron configuration through charge compensation but yields contrasting outcomes: Pd gives a small PL enhancement owing to reduced nonradiative loss, while Pt strongly quenches emission due to dominant nonradiative pathways despite strong spin–orbit coupling. Ni uniquely toggles between a distorted $6e^-$ open–shell and a symmetric $8e^-$ closed–shell state, with NIR emission peak position and intensity of the $8e^-$ state being similar to those of Ag_{25}. Overall, dopant identity dictates the balance between electron-count, orbital hybridization, and radiative *vs.* nonradiative decay, enabling a systematic control of emission energy and quantum yield in silver superatoms. The obtained mechanistic insights will benefit the applications of NCs in catalysis, optics, electronics, and sensing.

These dopant-dependent mechanisms enable rational tuning of NIR emission brightness and lifetime *via* control of k_r/k_{nr} and triplet-state involvement. Since NIR emission is deep tissue-penetrating and minimally photodamaging, the Ag_{25}/MAg_{24} family is promising for biosensing. In addition, such doped NCs are also attractive in energy catalysis,[41,42] photon upconversion,[43,44] solar cells,[45] nonlinear optics[46] and other applications. Future work will lead to exquisite tailoring for functional NCs with high performance for broader applications.

Conflicts of interest

The authors declare no conflicts of interest.

Data availability

The authors confirm that all the data supporting the findings of this study are available within the article and its supplementary information (SI). Supplementary information: experimental section (details of the synthesis and characterization including UV-vis-NIR absorption, steady-state and time-resolved photoluminescence, O_2 tests, and quantum-yield determination), and SI Fig. S1. See DOI: https://doi.org/10.1039/d5cp04426j.

Acknowledgements

R. J. acknowledges NSF funding (DMR 2419539), and U. T. thanks an Egyptian government fellowship.

References

1 Y. Li, M. Zhou, Y. Song, T. Higaki, H. Wang and R. Jin, *Nature*, 2021, **594**, 380–384.
2 S.-F. Yuan, C.-Q. Xu, W.-D. Liu, J.-X. Zhang, J. Li and Q.-M. Wang, *J. Am. Chem. Soc.*, 2021, **143**, 12261–12267.
3 Z. R. Yuan, Z. Wang, B. L. Han, C. K. Zhang, S. S. Zhang, Z. Y. Zhu, J. H. Yu, T. D. Li, Y. Z. Li, C. H. Tung and D. Sun, *Angew. Chem., Int. Ed.*, 2022, **61**, e202211628.
4 Y. Wang, C. Zhang, T. Xu, Y. Li, H. Xie, D. Sun, N. Feng, S. Li and X. Xin, *ACS Appl. Mater. Interfaces*, 2022, **17**, 17307–17315.
5 Y. Zhang, J. Zhang, Z. Li, Z. Qin, S. Sharma and G. Li, *Commun. Chem.*, 2023, **6**, 24.
6 Y. Liu, Z. Li, X.-H. Liu, N. Pinna and Y. Wang, *Nanoscale Horiz.*, 2023, **8**, 1435–1439.
7 L. Zhan, J. Zhang, B. Ning, Y. He, G. Xiao, Z. Chen and F.-X. Xiao, *Inorg. Chem. Front.*, 2024, **11**, 7991–8002.
8 L. Huang, R. Lu, W. Zhang, Y. Fan, Y. Du, K. Ni, Y. Zhu and M. Zhu, *Angew. Chem., Int. Ed.*, 2024, **63**, e202412964.
9 H. Seong, M. Choi, S. Park, H.-W. Kim, J. Kim, W. Kim, J. S. Yoo and D. Lee, *ACS Energy Lett.*, 2022, **7**, 4177–4184.
10 Z. Zhang, R. Yin, Z. Song, M. Zhang, B. Zhang, S. Lu, Q. Yao, D.-E. Jiang, J. Xie and W. Hu, *Angew. Chem., Int. Ed.*, 2025, **64**, e202500389.
11 X. Wei, C. Xu, H. Li, X. Kang and M. Zhu, *Chem. Sci.*, 2022, **13**, 5531–5538.

12 M. Zhu, C. M. Aikens, M. P. Hendrich, R. Gupta, H. Qian, G. C. Schatz and R. Jin, *J. Am. Chem. Soc.*, 2009, **131**, 2490–2492.
13 C. P. Joshi, M. S. Bootharaju, M. J. Alhilaly and O. M. Bakr, *J. Am. Chem. Soc.*, 2015, **137**, 11578–11581.
14 M. S. Bootharaju, C. P. Joshi, M. R. Parida, O. F. Mohammed and O. M. Bakr, *Angew. Chem.*, 2016, **128**, 934–938.
15 J. Yan, H. Su, H. Yang, S. Malola, S. Lin, H. Häkkinen and N. Zheng, *J. Am. Chem. Soc.*, 2015, **137**, 11880–11883.
16 M. Kim, K. L. D. M. Weerawardene, W. Choi, S. M. Han, J. Paik, Y. Kim, M.-G. Choi, C. M. Aikens and D. Lee, *Chem. Mater.*, 2020, **32**, 10216–10226.
17 M. Neumaier, A. Baksi, P. Weis, E. K. Schneider, P. Chakraborty, H. Hahn, T. Pradeep and M. M. Kappes, *J. Am. Chem. Soc.*, 2021, **143**, 6969–6980.
18 Q. Yuan, X. Kang, D. Hu, C. Qin, S. Wang and M. Zhu, *Dalton Trans.*, 2019, **48**, 13190–13196.
19 X. Liu, J. Yuan, C. Yao, J. Chen, L. Li, X. Bao, J. Yang and Z. Wu, *J. Phys. Chem. C*, 2017, **121**, 13848–13853.
20 H. Ji, M. Chen, Y. Sun, W. Liu, M. Jiang, Y. Liu, R. Qin, J. Liu, Z. Hao, F. Zhang, X. Li, L. Zhang and R. Zhang, *Sens. Actuators, B*, 2025, **439**, 137840.
21 S. Maity, S. Kolay, S. Ghosh, S. Chakraborty, D. Bain and A. Patra, *J. Phys. Chem. Lett.*, 2022, **13**, 5581–5588.
22 P. D'Antoni, L. Sementa, S. Bonacchi, M. Reato, F. Maran, A. Fortunelli and M. Stener, *Phys. Chem. Chem. Phys.*, 2024, **26**, 17569–17576.
23 F. Alkan, P. Pandeya and C. M. Aikens, *J. Phys. Chem. C*, 2019, **123**, 9516–9527.
24 H. Liu, B. Huang, Y. Shao and Y. Pei, *Small*, 2024, **20**, e2403520.
25 E. Wang and Y. Gao, *J. Cluster Sci.*, 2025, **36**, 115.
26 K. L. Dimuthu, M. Weerawardene and C. M. Aikens, *J. Phys. Chem. C*, 2018, **122**, 2440–2447.
27 A. Tlahuice-Flores, *Mol. Simul.*, 2013, **39**, 428–431.
28 H. Yi, S. Song, S. M. Han, J. Lee, W. Kim, E. Sim and D. Lee, *Angew. Chem., Int. Ed.*, 2023, **62**, e202302591.
29 Y. Wang, Z. Liu, A. Mazumder, C. G. Gianopoulos, K. Kirschbaum, L. A. Peteanu and R. Jin, *J. Am. Chem. Soc.*, 2023, **145**, 26328–26338.
30 Z. Liu, M. Zhou, L. Luo, Y. Wang, E. Kahng and R. Jin, *J. Am. Chem. Soc.*, 2023, **145**, 19969–19981.
31 A. A. A. Ahmed, S. Havenridge, K. Sahoo, L. Thapa, A. Baksi, G. H. Clever, H. Noei, M. Kohantorabi, A. Stierle, C. R. Raj, W. J. Parak, C. M. Aikens and I. Chakraborty, *Small*, 2024, **21**, 2408096.
32 A. Pniakowska, K. K. Ramankutty, P. Obstarczyk, M. Perić Bakulić, Ž. Sanader Maršić, V. Bonačić-Koutecký, T. Bürgi and J. Olesiak-Bańska, *Angew. Chem., Int. Ed.*, 2022, **61**, e202209645.
33 Y. Yu, Z. Luo, D. M. Chevrier, D. T. Leong, P. Zhang, D.-E. Jiang and J. Xie, *J. Am. Chem. Soc.*, 2014, **136**, 1246–1249.
34 P. A. Lummis, K. M. Osten, T. I. Levchenko, M. Sabooni, A. Hazer, S. Malola, B. Owens-Baird, A. J. Veinot, E. L. Albright, G. Schatte, S. Takano, K. Kovnir, K. G. Stamplecoskie, T. Tsukuda, H. Häkkinen, M. Nambo and C. M. Crudden, *JACS Au*, 2022, **2**, 875–885.
35 S. Maity, D. Bain and A. Patra, *Nanoscale*, 2019, **11**, 22685–22723.
36 M. Mitsui, D. Arima, A. Uchida, K. Yoshida, Y. Arai, K. Kawasaki and Y. Niihori, *J. Phys. Chem. Lett.*, 2022, **13**, 9272–9278.
37 S. Takano, H. Hirai, T. Nakashima, T. Iwasa, T. Taketsugu and T. Tsukuda, *J. Am. Chem. Soc.*, 2021, **143**, 10560–10564.
38 L. Luo, Z. Liu, X. Du and R. Jin, *J. Am. Chem. Soc.*, 2022, **144**, 19243–19247.
39 L. Luo, Z. Liu, A. Mazumder and R. Jin, *J. Am. Chem. Soc.*, 2024, **146**, 27993–27997.
40 W. Fan, Y. Yang, Q. You, J. Li, H. Deng, N. Yan and Z. Wu, *J. Phys. Chem. C*, 2023, **127**, 816–823.
41 K. Kwak and D. Lee, *Acc. Chem. Res.*, 2019, **52**, 12–22.
42 S. Li, A. V. Nagarajan, S. Zhao, G. Mpourmpakis and R. Jin, *J. Phys. Chem. C*, 2021, **125**, 24831–24836.
43 Y. Niihori, Y. Wada and M. Mitsui, *Angew. Chem., Int. Ed.*, 2021, **60**, 2822–2827.
44 Z. Liu, X. Hu, L. Luo, G. He, A. Mazumder, E. Gunay, Y. Wang, E. C. Dickey, L. A. Peteanu, K. Matyjaszewski and R. Jin, *J. Am. Chem. Soc.*, 2025, **147**, 28241–28250.
45 M. S. Kim, M. A. Abbas and J. H. Bang, *Bull. Korean Chem. Soc.*, 2016, **37**, 791–792.
46 R. Antoine and V. Bonacic-Koutecky, *Liganded Silver and Gold Quantum Clusters. Towards a New Class of Nonlinear Optical Nanomaterials*. Springer, 2018.

